Searching for Spinning Black Hole Binaries in Advanced LIGO and Virgo

LIGO Caltech SURF 2013

Deborah L. Hamm

Mentors: Stephen Privitera, Alan Weinstein

October 11, 2013

Abstract

A promising source of gravitational waves (GWs), detectable by LIGO and VIRGO observatories, are coalescing binary black holes (BBHs). Searches for coalescing BBHs employ the technique of matched filtering in which theoretical predictions of the waveform signal are used to filter the data. Therefore, these searches rely crucially on an accurate GW model for detection. BHs in binaries may have significant spins and the effect of spin is encoded in the waveform. Here we explore the benefits of including the effects of spin aligned with orbital angular momentum in the search of GWs from coalescing BBHs. We show that for the advanced LIGO high power zero-detuned sensitivity in the mass range of $[40, 125]M_{\odot}$ and for effective spin $\chi \in [0.0, 0.85]$ the inclusion of spin-aligned effects can increase the mean sensitive distance by up to $\sim 40\%$

1 Overview

The detection of GWs will serve as a new probe into the universe with possibilities for bringing insight into some of the most interesting questions in

physics and astronomy. Because of the weak interaction of GWs with matter the astronomical sources for GW detection are required to be extremely luminous in gravitational radiation [1]. Of particular interest to the LIGO community is the coalescing binary black hole (BBH) system whose gravitational waveform should be readily detectable by ground based detectors.

Coalescing BBHs evolve through three distinct phases: the *inspiral*, *merger*, and *ringdown* phases (IMR). The *inspiral* phase ends once the system has reached the innermost stable circular orbit (ISCO). The *merger* phase occurs when the bodies combine, colliding at near the speed of light, into a single BH[2]. The *ringdown* phase is the result of asymmetry in the resultant single BH. From this asymmetry, the BH emits gravitational radiation until it decays into a stationary Kerr state. The gravitational radiation it emits is dependent upon the mass and spin of the final BH[3]. Imprinted onto the GW are the BH's mass, spin, sky location, and distance from Earth[4].

The core technique in GW data pipeline processing for searches of compact binaries is the use of matched filtering[1]. Post-Newtonian (PN) and numerical relativity (NR) techniques are employed to create waveform templates from the predictions of GWs for CBCs. Computationally generated over a range of binary component parameter space, these waveform templates are utilized as filters for the data stream of a detector. Overlap between a waveform template in the filter and a waveform from the data stream, that reaches a certain threshold, will result in a potential detection. Matched filtering is the optimal approach to successful detections with Gaussian-distributed background noise.

It is expected that BBHs in nature will have significant spin. Of those that evolve in isolation, it is thought that they will have significant $non-precessing$ spin (spin aligned with orbital angular momentum). Therefore, including spin effects in our matched template filters becomes a necessity in order to effectively detect these gravitational waveforms.

Previously, the only template banks available to the gravitational wave community were ones in which the model waveforms did not include the effects of spin. Eventually, other waveform models became available that included spin for the inspiral phase *only*. In 2008, results were published on the first data search (LIGO's science run 3) for GWs from CBCs that included the effects of spin-induced orbital precession for the inspiral phase [5]. In 2013, results were published on a search for GW signals

from coalescence of high-mass BBHs without spin of data from LIGO's sixth science run (S6) and Virgo's second (VSR2) and third (VSR3) science runs. The data were match filtered against a template bank of waveforms, called EOBNRv1, that included all three phases of coalescence but without including the effects of spin. As part of their results, an evaluation of sensitivity was performed using the IMRPhenomB waveform family that included spin-aligned effects[6] for all three phases. It was found that there was a loss in sensitivity for injections with spin most likely due to a reduction in overlap of the EOBNRv1 templates with the simulated IMRPhenomB injections[6].

New to the gravitational wave community are template models that include aligned spin for all three phases (IMR). While the inspiral and ringdown stages of the BBH coalescence can be modeled analytically, the merger stages must be modeled numerically[7]. Therefore, to construct a template waveform that includes all three stages, both the analytical and numerical models must be combined[7]. The addition of spin to these models contributes an additional six parameters (three for each BH). This leads to significantly higher SNR[7].

2 Effectualness of Template Banks without Spin for Detecting Signals with Spin

2.1 IMRPhenomB

The waveform family considered for this study is a phenomenological fit to the post-Newtonian (PN) and numerical relativity (NR) hybrid waveforms outlined in [7]. They cover all three phases of coalescence, include the effects of aligned spin, and are collectively called IMRPhenomB.

Degeneracies in the physical parameters [7] allow IMRPhenomB to be parameterized by only the total mass of the binary

$$M \equiv m_1 + m_2,$$

the symmetric mass ratio

$$\eta \equiv m_1 m_2 / M^2,$$

and a *single* spin parameter, or *effective* spin χ, where

$$\chi \equiv \frac{a_1 m_1 + a_2 m_2}{M},$$

and

$$a_i \equiv S_i / m_i^2,$$

with S_i the spin angular momentum of the ith BH[7]. In equal mass systems, χ (in the physical range from -1 to 1) is the dominant spin effect on the waveform and is the mass-weighted total spin of the system [7].

2.2 Constructing a Template Bank

Our template filter bank contains IMRPhenomB waveforms that cover a discrete range of parameters to filter GW data that covers a continuous range of parameter space. For our parameters we consider the masses of the binary components and the effective spin parameter χ. IMRPhenomB is expected to be accurate only for low to moderate mass ratios and spins [8]. We therefore restrict our study to mass ratios of $1 \leq \frac{m_1}{m_2} \leq 4$ and $\chi \in [-0.5, 0.85]$.

We used a stochastic method to construct our template bank in which templates are proposed to the bank randomly. Let a template bank be denoted by $B = \{\hat{h_i}\}_{i=1}^{N}$, and $\hat{h_1}$ be a normalized waveform so that $\langle \hat{h_1} | \hat{h_1} \rangle = 1$. A target waveform with arbitrary source parameters is given by $\hat{h}_{\vec{\lambda}}$. Then, overlap between waveforms in the bank and waveforms proposed to the bank is measured by a *fitting factor*,

$$FF(\vec{\lambda}; B) = max_{i,t} \langle \hat{h}_i | \hat{h}_{\vec{\lambda}} \rangle,$$

maximized over all templates in the bank and over all time translations [8]. Arbitrary source parameters (target waveofms) are indicated by $\vec{\lambda}$. For our template bank to be considered an effectual filter of signal it must achieve a mean fitting factor (MFF) of 0.97 with our target waveforms, where our target waveforms are considered.

2.3 Non-Spinning Template Filter Bank vs. Spinning Templates

In order to determine the parameter space in which including the effects of spin in our filter template bank would be most effective we calculated the MFF for a non-spin bank against spinning target waveforms. Our template mass range was $M \in [40, 350]M_{\odot}$. We chose a low frequency cutoff of $f = 10$ Hz due to a sharp rise in noise in the advanced LIGO sensitivity curves (figure 1). For our target waveforms we cover the same mass range and a χ range of $[-0.5, 0.85]$.

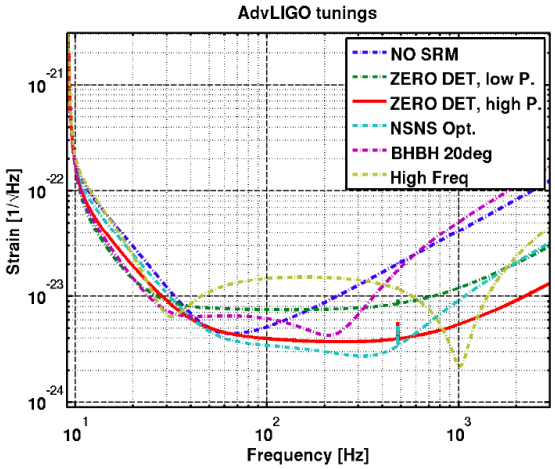

Figure 1: Advanced LIGO total noise curves for different configurations.

In figure 2 we show the MFF as a function of the total mass of the binary and the *effective* spin χ. The MFF is a direct measure of recoverable signal-to-noise-ratio (SNR, see appendix). Figure 2 shows that for systems with negative values of χ there is no significant loss in SNR with a non-spin bank. Also, for systems with positive χ values and larger total mass ($\gtrsim$

150 $M_\odot$), the loss of SNR decreases. We therefore choose to focus further study on systems where $\chi \in [0.0, 0.85]$ and $M \in [40.0, 125] M_\odot$.

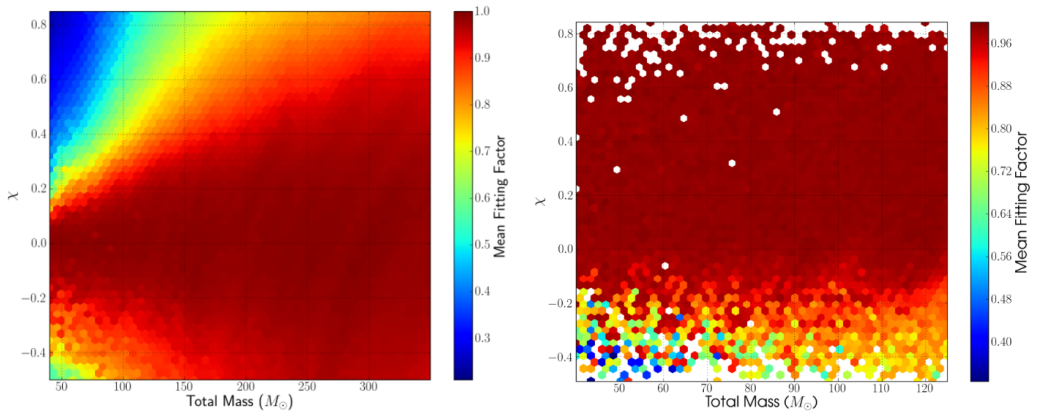

(a) (b)

Figure 2: For a non-spin template bank (a) systems with negative χ values are captured. With increasing total mass and positive χ values (a) the amount of recoverable SNR decreases. The greatest amount of recoverable SNR lies in the total mass region $M \in [40.0, 125]$ and $\chi \in [0.0, 0.85]$ (a). Focusing on this region, a template bank with $\chi \in [0.0, 0.85]$ captures systems with positive aligned spin (b).

3 Search Sensitivity Improvement with Spin-aligned Templates

A study was performed characterizing the effectiveness of a nonspin bank vs. a spin bank from within a search pipeline. The noise spectrum utilized (figure 1) was aLigoHighPowerZeroDetuned with Gaussian distributed background.

Including the effects of spin increases the number of templates in a filter bank. The increase in the number of templates from our non-spin bank ($\sim$ 1200) to our spin-bank ($\sim$ 6000) was a factor of $\sim$ 5. More templates increases the number of false alarm triggers when filtering signal plus noise. The number of false alarm triggers is proportional to the FAR by,

$$N_{bg} \simeq N_{templates} e^{-\rho^2}.$$

By including the effects of spin in our filter bank, the number of false alarm triggers increased by a factor of ~ 3 (figure 3). Therefore, it is expected that gains in SNR will be offset by losses due to an increased FAR.

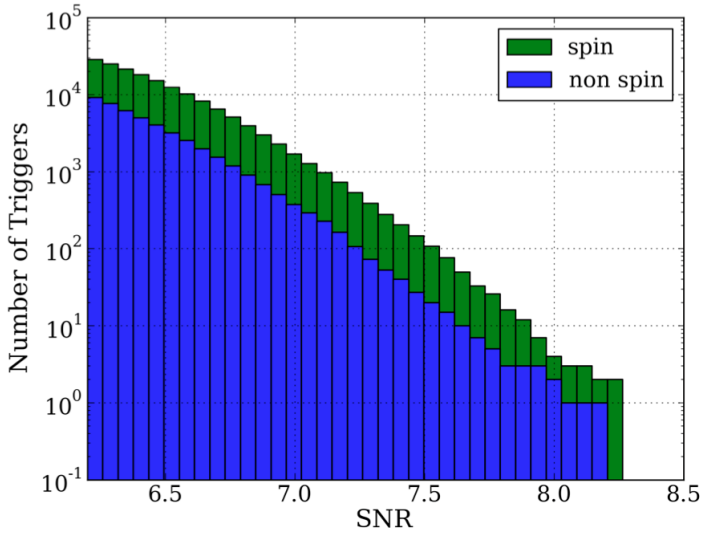

Figure 3: The number of templates in our spin bank increased by a factor of ~ 5 from our non-spin bank. More templates translates into an increase in the number of false alarm triggers. Our results show that for a spin-bank the increase in false alarm triggers is ~ 3.

Figure 4 shows our results for the mean sensitive distance as a function of the FAR. For $\chi \in [0.0, 0.2]$ we see very little variation between the performance of a non-spin bank compared to a spin bank throughout a mass range of $M \in [60, 100.0]M_{\odot}$ (figures 4(a) and 4(b)). This indicates an apparently coincidental offset of SNR gains to losses due to an increased FAR. For $\chi \in [0.2, 0.5]$ and mass range $M \in [60.0, 80.0]M_{\odot}$ we see a difference between the performance of a non-spin bank and a spin bank with an increase in mean sensitive distance by $\sim 7\%$ (figure 4(c)). For $\chi \in [0.5, 0.85]$ the increase in mean sensitive distance is $\sim 40\%$ for $M \in [60.0, 80.0]M_{\odot}$ at low FAR (figures 4d,e,f).

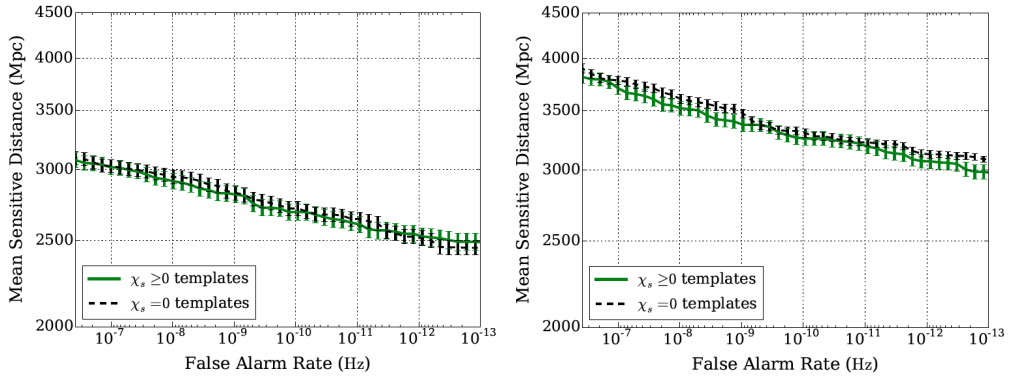

(a) $\chi \in [0.0, 0.2]$; $M \in [60.0, 80.0] M_\odot$ (b) $\chi \in [0.0, 0.2]$; $M \in [80.0, 100.0] M_\odot$

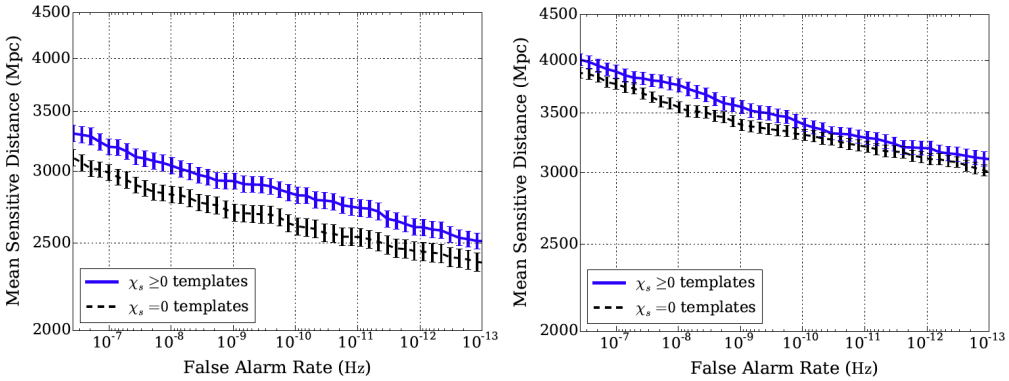

(c) $\chi \in [0.2, 0.5]$; $M \in [60.0, 80.0] M_\odot$ (d) $\chi \in [0.2, 0.5]$; $M \in [80.0, 100.0] M_\odot$

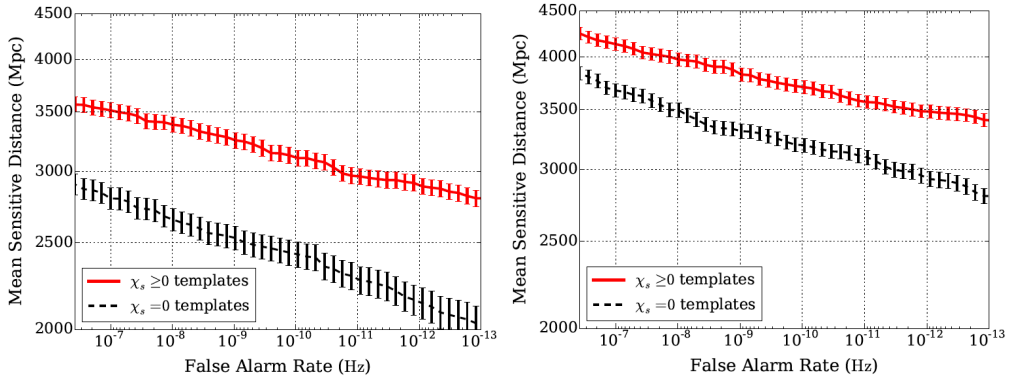

(e) $\chi \in [0.5, 0.85]$; $M \in [60.0, 80.0] M_\odot$ (f) $\chi \in [0.5, 0.85]$; $M \in [80.0, 100.0] M_\odot$

Figure 4: Gains in SNR are perfectly offset by losses due to an increased FAR with $\chi \in [0.0, 0.2]$ (a),(b) with no differentiation between the non-spin and spin banks. For $\chi \in [0.2, 0.5]$ only slight gains in mean sensitive distance are achieved ($\sim 7\%$) for our lower mass systems with a spin bank (c), with $\sim 5\%$ achieved for the higher mass (d). Highest gains are with $\chi \in [0.5, 0.85]$ (e),(f). The highest mass systems achieve a gain of $\sim 25\%$ at low FAR (f). The lower mass systems achieve a gain of ($\sim 40\%$) at low FAR (e).

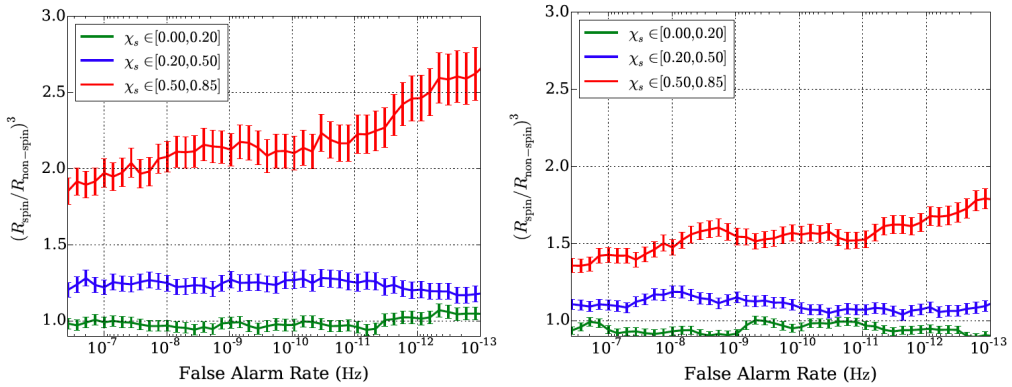

(a) $M \in [60.0, 80.0]M_{\odot}$ (b) $M \in [80.0, 100.0]M_{\odot}$

Figure 5: The ratio of the sensitive volumes of the template bank including the effects of spin to the template bank without spin indicate nearly identical sensitivities for low values of χ.

As discussed in section 2.3, the MFF is a measure of recoverable SNR. SNR scales inversely with the distance to a signal's source [8] and the detection rate scales as the cube of the sensitive distance [8]. We can therefore define the fractional increase in detection rate resulting from the inclusion of spin in our template bank by

$$\frac{V_{spin}}{V_{nonspin}} = \left(\frac{FF_{spin}}{FF_{nonspin}} \right)^3,$$

where FF_{spin} and $FF_{nonspin}$ are the fitting factors for the spinning and non-spinning template banks with target waveforms [8].

Our results (figure 5) show that for low χ values the sensitivities achieved are nearly identical as expected. For higher values of χ, and especially for the lower mass range, the template bank including aligned spin has significantly higher volume sensitivity for a fixed FAR.

Two methods of background rejection were employed for this study. First, H1 and L1 shared the same template filter bank. For a trigger in H1 and a trigger in L1 to be considered coincident, they must ring up the exact same template in the bank.

Second, an auto-correlation signal consistency test denoted as χ^2 (not to be confused with the effective spin parameter χ) measured how consistent our data was with Gaussian distributed noise plus signal. Figure 6 shows results for SNR (ρ) and χ^2 values for both the non-spin bank and the spin bank. High χ^2 values for injections indicate a loss in discrimination between noise and signal. The non-spin bank (figure 5a) results in much higher χ^2 values than the spin bank (figure 5b) by more than a factor of 10 at SNR $\sim$ 100 and a factor of $\sim$ 3 at SNR $\sim$ 10.

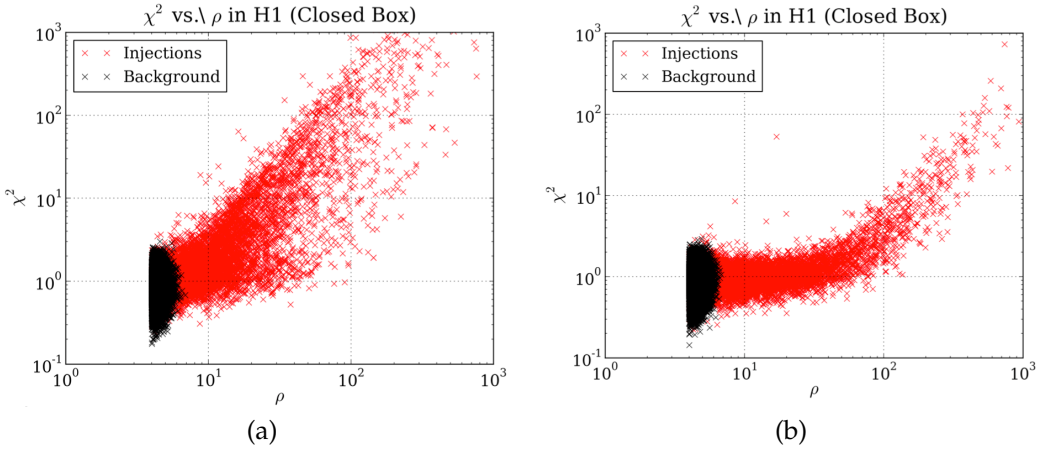

(a) (b)

Figure 6: On the following plots, our data points are instances of injection and background detector triggers. Red represents software injections, while data in black represents our background. Higher χ^2 values indicate poor discrimination between noise and signal. The non-spin bank (a) indicates poor discrimination between noise and signal as compared to our spin bank (b) by a factor of $\sim$ 3 to a factor of $\sim$ 10 at SNRs $\sim$ 10 and $\sim$ 100 respectively.

4 Parameter Recovery

To leading order, the phase and amplitude (see appendix IMRPhenomB) of the GW depend on the *chirp mass* ($\mathcal{M}_{chirp}$). Where

$$\mathcal{M}_{chirp} = M\eta^{\frac{3}{5}},$$

and $M = m_1 + m_2$ is the total mass and $\eta = \frac{m_1 m_2}{M^2}$. SNR scales with the *chirp mass* as

$$\rho \propto \frac{\mathcal{M}^{\frac{5}{6}}}{d},$$

where d is the distance to the binary [9].

Our results (figure 7) show fractional $\mathcal{M}_{chirp}$ recovery to be systematically biased to lower values with increasing values of χ (figure 7a) for our non-spin bank. Higher mass systems with high values for χ may match with lower mass templates in the non-spin bank with the result being a less accurate parameter recovery. While our spin bank (figure 7b) has very accurate and unbiased recovery covering all χ values.

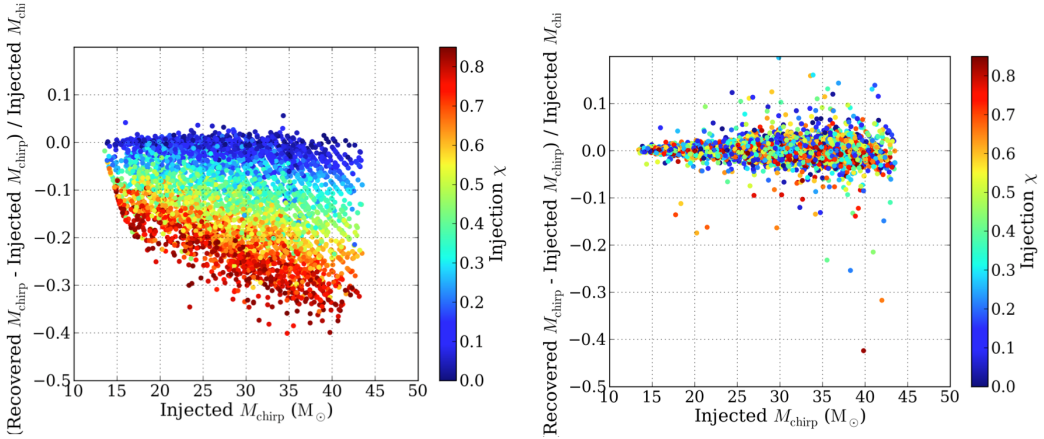

(a) (b)

Figure 7: There is a significant bias in $\mathcal{M}_{chirp}$ recovery with increasing values of χ for a template bank that does not include the effects of spin (a). Including the effects of spin allows for greater accuracy over the entire range of χ values (b).

5 Future Work

5.1 IMRPhenomB Waveform Limitations

IMRPhenomB waveforms are constrained by $fM > 400$ where f is the low frequency cutoff in Hz and M is the total mass of the binary in solar

masses [7]. This limits the lower mass range of templates available. In order to cover a lower mass search the low frequency cutoff would need to be increased thereby disallowing the utilization of the full sensitive frequency band of the advanced detectors. Boundary effects can be seen at the edges of the parameter space in which IMRPhenomB waveforms are reliable for lower mass highly spinning systems (figures 8c, 9).

The next generation of waveforms, IMRPhenomC, represents a step forward in theoretical waveform modeling that can cover the entire mass range without this constraint [7].

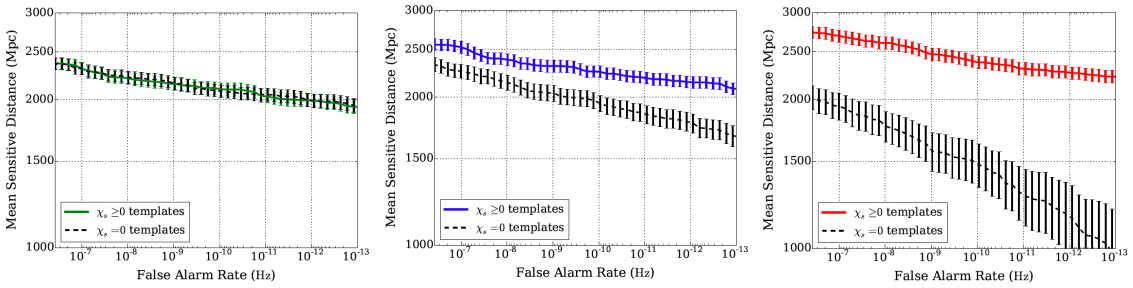

(a) $M \in [40.0, 60.0]M_\odot$ (b) $M \in [40.0, 60.0]M_\odot$ (c) $M \in [40.0, 60.0]M_\odot$

Figure 8: For systems with a total mass range of $M \in [40.0, 60.0]M_\odot$ and low values of χ the mean sensitive distance is nearly identical for a spinning and non-spinning template banks (a). There is an improvement in mean sensitive distance when including the effects of spin in the template bank for systems with moderate spin (b). With a low frequency cutoff of 10 Hz, over the mass range $M \in [40.0, 60.0]M_\odot$ there are boundary effects due to the $fM > 400$ constraint on the IMRPhenomB waveform family (c).

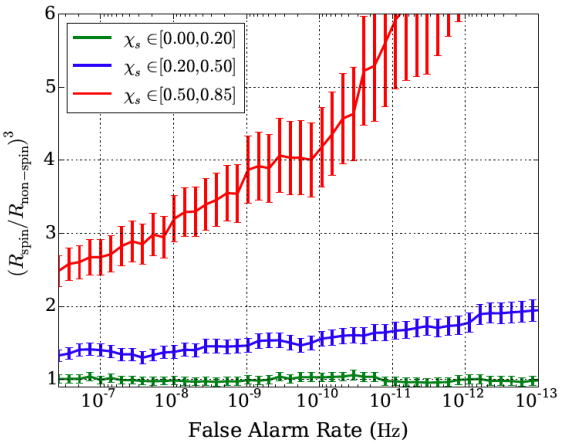

Figure 9: The boundary effects of the IMRPhenomB waveform family are evident in the ratio of the sensitive volumes for systems with high values of χ.

6 Appendix

6.1 Signal to Noise Ratio

Given data stream $\tilde{s}(f) = \tilde{n}(f) + \tilde{h}(f)$, where $\tilde{n}(f)$ is detector noise and $\tilde{h}(f)$ is signal, the equation for the *amplitude* SNR of the (quadrature) matched filter is [10]:

$$\rho_m(t) = \frac{|z_m(t)|}{\sigma_m}.$$

Where a measure of the sensitivity of the instrument is given by σ_m^2

$$\sigma_m^2 = 4 \int_0^\infty \frac{|\tilde{h}_{1Mpc,m}(f)|^2}{S_n(f)} df,$$

and $z(t)$ is the complex matched filter output, with one-sided power spectral density $S_n(f)$, given by

$$z(t) = x(t) + iy(t) = 4 \int_0^\infty \frac{\tilde{s}(f)\tilde{h}^\star_{template}(f)}{S_n(f)} e^{2\pi i f t} df,$$

with $x(t)$ the matched filter output of the data stream

$$x(t) = 4Re \int_0^\infty \frac{\tilde{s}(f)\tilde{h}^\star_{template}(f)}{S_n(f)} e^{2\pi i f t} df,$$

and $y(t)$ the matched filter output of the template $\tilde{h}_{template}, 2\phi_0 \rightarrow 2\phi_0 - \frac{\pi}{2}(f) = \tilde{h}_{template}(f)e^{i\frac{pi}{2}} = i\tilde{h}_{template}(f)$ [10].

6.2 IMRPhenomB Waveform Family

IMRPhenomB waveforms are a phenomenological fit to PN and NR waveforms. The PN waveforms are most accurate during the inspiral phase of coalescence and become less accurate closer to merger. Breakdown of the PN waveforms occurs near the innermost stable circular orbit (ISCO) at the ultra-relativistic regime. There is a high computational cost for modelling inspiral phase NR waveforms with the best computational efficiency and accuracy for the late inspiral, merger, and ringdown phases. Information on the phase or Ψ of our waveform is critical in the matched filtering process. Considered here, the inspiral phase of our PN waveform in the frequency domain ($\tilde{h}(f)$) [10] is:

$$\begin{aligned}\tilde{h}(f) &= -\left(\frac{5\pi}{24}\right)^{1/2} \left(\frac{G\mathcal{M}}{c^3}\right) \left(\frac{G\mathcal{M}}{c^2 D_{eff}}\right) \left(\frac{G\mathcal{M}}{c^3}\pi f\right)^{-7/6} e^{-i\Psi(f;M,u)} \\ &= \left(\frac{1Mpc}{D_{eff}}\right) \mathcal{A}_{1Mpc}(M,\mu) f^{-7/6} e^{-i\Psi(f;M,\mu)}\end{aligned}$$

where

$$\mathcal{A}_{1Mpc}(M,\mu) = -\left(\frac{5}{24\pi}\right)^{1/2}\left(\frac{GM_\odot/c^2}{1Mpc}\right)\left(\frac{\pi GM_\odot}{c^3}\right)^{-1/6}\left(\frac{\mathcal{M}}{M_\odot}\right)^{-5/6},$$

$$\begin{aligned}\Psi(f;M,\mu) = {} & 2\pi f t_0 - 2\phi_0 - \pi/4 \\ & + \frac{3}{128\eta}[v^{-5} + \left(\frac{3715}{756} + \frac{55}{9}\eta\right)v^{-3} - 16\pi v^{-2} \\ & + \left(\frac{15294365}{508032} + \frac{27145}{504}\eta + \frac{3085}{72}\eta^2\right)v^{-1}],\end{aligned}$$

$$v = \left(\frac{GM}{c^3}\pi f\right)^{1/3},$$

where $\mathcal{M}$ is the chirp mass (defined in section 4), $M_\odot$ is the solar mass $\sim 2\times10^{30}$ kg, t_0 is the time at the detector at which the coalescence occurs, $\mu \equiv \frac{m_1 m_2}{M}$ is the reduced mass [10], and v is the relative orbital velocity of the binary.

Note that Ψ has been expanded to the second post-Newtonian order. It has been noted in [10] that the truncation of the series expansion will lead to errors in matching PN waveforms to the waveforms that nature gives us.

For IMRPhenomB, the inspiral phase is matched (from above) to the 2PN accurate adiabatic inspiral waveforms in the test-mass ($\eta \to 0$) limit [7] with resulting phase modelled as

$$\Psi = 2\pi f t_0 + \psi_0 + \frac{3}{128\eta} v^{-5} \left\{ 1 + \left(\frac{3715}{756} - 920.9\eta + 492.1\eta\chi + 135\eta\chi^2 + 6742\eta^2 \right.\right.$$
$$\left. - 1053\eta^2\chi - 1.4310^4\eta^3 \right) v^2 + \left(\frac{113}{12}\chi_s + \frac{113}{12}\delta\chi_a - 16\pi + 1.7021 0^4\eta \right.$$
$$\left. - 9566\eta\chi - 2182\eta\chi^2 - 1.2141 0^5\eta^2 + 2.0751 0^4\eta^2\chi + 2.3861 0^5\eta^3 \right) v^3$$
$$+ \left(\frac{15293365}{508032} - 10\chi_a^2\frac{81}{16} + \frac{810}{8}\chi_a\chi_s\delta + 10\chi_s^2\frac{81}{16} - 1.2541 0^5\eta + 7.5071 0^4\eta\chi \right.$$
$$\left. + 1.3381 0^4\eta\chi^2 + 8.7351 0^5\eta^2 - 1.6571 0^5\eta^2\chi - 1.6941 0^6\eta^3 \right) v^4$$
$$+ \left(\frac{6848}{21}\gamma_E - \frac{640}{3}\pi^2 + \frac{11583231236531}{4694215680} - \frac{6848}{21}\ln 4v - 8.8981 0^5\eta \right.$$
$$+ 6.311 0^5\eta\chi + 5.0681 0^4\eta\chi^2 + 5.9811 0^6\eta^2 - 1.4151 0^6\eta^2\chi$$
$$\left. - 1.1281 0^7\eta^3 \right) v^6 + \left(\frac{77 - 96675}{254016}\pi + 8.6961 0^5\eta - 6.711 0^5\eta\chi \right.$$
$$\left. \left. - 3.0081 0^4\eta\chi^2 - 5.8381 0^6\eta^2 + 1.5141 0^6\eta^2\chi + 1.0891 0^7\eta^3 \right) v^7 \right\} \tag{1}$$

7 Acknowledgements

Thanks to my LIGO mentors Stephen Privitera and Alan Weinstein, my NAU mentors David Trilling, Kathy Eastwood, and Mark James. Thanks to NSF for funding, the LIGO Surf Program, and the California Institute of Technology.

References

[1] Physics, Astrophysics and Cosmology with Gravitational Waves, B.S. Sathyaprakash, `http://relativity.livingreviews.org/Articles/lrr-2009-2/`

[2] LIGO: The Laser Interferometer Gravitational-Wave Observatory, pg. 16, the LIGO Scientific Collaboration, Rep. Prog. Phys. 72 (2009) 076901

[3] Cardiff University School of Physics and Astronomy website: http://www.astro.cardiff.ac.uk/research/gravity/tutorial/?page=4blackholecollisions

[4] LIGO Scientific Collaboration website: http://www.ligo.org/science/Publication-S6PE/index.php

[5] Search of LIGO data for gravitational wave signals from spinning black hole and neutron star binary inspirals, arXiv:0712.2050v3 [gr-qc] 30 June 2008

[6] Search for Gravitational Waves from Binary Black Hole Inspiral, Merger, and Ringdown in LIGO-Virgo Data from 2009-2010, arXiv:1209.6533v3 [gr-qc] 25 Feb 2013

[7] IMR waveforms for BBH with non-precessing spins, P. Ajith, arXiv:0909.2867v3 [gr-qc] 8 Jun 2011

[8] Improving the sensitivity of a search for coalescing binary black holes with non-precessing in gravitational wave data, S. Privitera, LIGO DCC: P1200132-x0

[9] Searching for Gravitational Waves from Binary Inspirals with LIGO, D. Brown, arXiv:0705.1572v1 [gr-qc] 11 May 2007

[10] FINDCHIRP: an algorithm for detection of gravitational waves from inspiraling compact binaries, B. Allen, arXiv:gr-qc/0509116v2 4 Aug 11